



Droplet evaporation in finite-size systems: Theoretical analysis and mesoscopic modelingLinlin Fei ^{1,*}, Feifei Qin ¹, Geng Wang,² Kai H. Luo,² Dominique Derome,³ and Jan Carmeliet¹¹*Chair of Building Physics, Department of Mechanical and Process Engineering, ETH Zürich (Swiss Federal Institute of Technology in Zürich), Zürich 8092, Switzerland*²*Department of Mechanical Engineering, University College London, Torrington Place, London WC1E 7JE, United Kingdom*³*Department of Civil and Building Engineering, Université de Sherbrooke, Sherbrooke, QC J1K 2R1, Canada*

(Received 18 October 2021; accepted 17 January 2022; published 3 February 2022)

The classical D^2 -Law states that the square of the droplet diameter decreases linearly with time during its evaporation process, i.e., $D^2(t) = D_0^2 - Kt$, where D_0 is the droplet initial diameter and K is the evaporation constant. Though the law has been widely verified by experiments, considerable deviations are observed in many cases. In this work, a revised theoretical analysis of the single droplet evaporation in finite-size open systems is presented for both two-dimensional (2D) and 3D cases. Our analysis shows that the classical D^2 -Law is only applicable for 3D large systems ($L \gg D_0$, L is the system size), while significant deviations occur for small ($L \leq 5D_0$) and/or 2D systems. Theoretical solution for the temperature field is also derived. Moreover, we discuss in detail the proper numerical implementation of droplet evaporation in finite-size open systems by the mesoscopic lattice Boltzmann method (LBM). Taking into consideration shrinkage effects and an adaptive pressure boundary condition, droplet evaporation in finite-size 2D/3D systems with density ratio up to 328 within a wide parameter range ($K = [0.003, 0.18]$ in lattice units) is simulated, and remarkable agreement with the theoretical solution is achieved, in contrast to previous simulations. The present work provides insights into realistic droplet evaporation phenomena and their numerical modeling using diffuse-interface methods.

DOI: [10.1103/PhysRevE.105.025101](https://doi.org/10.1103/PhysRevE.105.025101)**I. INTRODUCTION**

Droplet evaporation is ubiquitous in various engineering applications, natural phenomena, and pathological situations, ranging from spray combustion in the internal combustion engines [1], drying of raindrops on the surface of building materials [2], to the spread of virus-laden droplets during the COVID-19 pandemic [3]. Understanding the detailed droplet evaporation dynamics helps to accurately predict the evaporation rate and the droplet lifetime, and is beneficial to the advancement of many fields of science and technology.

Though different complex factors are involved in realistic droplet evaporation processes, such as multicomponent diffusion [4], relative motion between droplet and surrounding gas [5], nanoparticle deposition [6,7], and contact line pinning/depinning [8,9], it is worth investigating basic cases as a first step. One canonical configuration is the single-component single static droplet evaporation in an open system. Such evaporation is symmetrically driven by the temperature gradient from the liquid-vapor interface (T_s) to the far-field (T_∞). Assuming the process is quasisteady, the thermophysical properties are spatially uniform, and viscous heat dissipation and buoyancy can be neglected, thus the following relation can be obtained based on the energy balance at the interface [1,10]:

$$D^2(t) = D_0^2 - K_T t, \quad (1)$$

where D_0 is the droplet initial diameter and $K_T = \frac{8\lambda}{\rho_l c_p} \ln(1 + B_T)$ is the evaporation constant, depending on thermal conductivity λ , liquid density ρ_l , specific heat capacity c_p , and the Spalding number B_T . The nondimensional Spalding number B_T is the ratio of sensible heat to the latent heat (h_{fg}) of the droplet fluid, i.e., $B_T = c_p(T_\infty - T_s)/h_{fg}$. Another important configuration is the two-component isothermal evaporation for a single static droplet in the surrounding gas mixture (droplet vapor and environment air), where the evaporation is driven by the vapor concentration gradient from the environment to the droplet surface. Similarly, under the assumptions of quasisteady evaporation with constant thermo-physical properties and noncondensation of the environment air, another relation can be derived based on the mass balance at the interface [1,10]:

$$D^2(t) = D_0^2 - K_Y t, \quad (2)$$

where the evaporation constant K_Y depends on the product of gas mixture density and the binary diffusivity ρD , liquid density ρ_l , and the mass transfer number B_Y by $K_Y = \frac{8\rho D}{\rho_l} \ln(1 + B_Y)$. The mass transfer number B_Y is related to the mass concentration of the droplet vapor at the interface Y_s and the environment Y_∞ , i.e., $B_Y = (Y_s - Y_\infty)/(1 - Y_s)$. It is noted Eq. (2) is quite similar to Eq. (1): apart from the difference between the mass transfer number B_Y and the Spalding number B_T , the two relations show essentially the same form and become the same equation if the Lewis number is unity ($\lambda/c_p = \rho D$). Therefore, a more compact expression with unified evaporation constant K is often used in the

*Corresponding author: linfei@ethz.ch

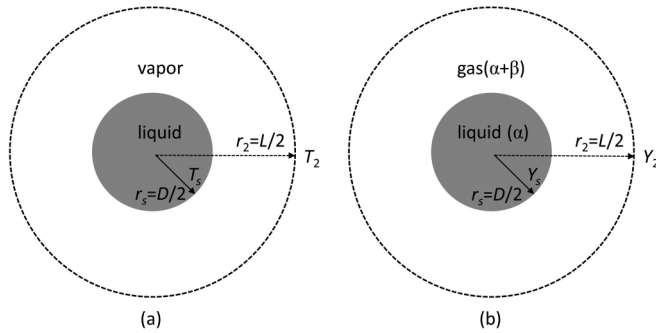


FIG. 1. 3D mid-plane or 2D schematic view of single static droplet evaporation in a finite-size open system: (a) single component evaporation driven by temperature gradient and (b) two-component isothermal evaporation driven by the concentration gradient.

literature, namely $D^2(t) = D_0^2 - Kt$, which is also known as the so-called D^2 -Law [1,10]. It was demonstrated in experiments that, after a short initial stage, D^2 -Law works well for the evaporation of fuel droplets at various ambient air temperatures [11]. Accordingly, the droplet lifetime is estimated as $t_d = D_0^2/K$. Droplet evaporation under more complex conditions can be modeled step by step starting from the classical D^2 -Law model [4,5,12].

Deviations from the classical D^2 -Law have been frequently observed, especially in droplet evaporation experiments in confined space [13] or in numerical simulations, e.g., evaporation of nanosize droplets and/or under supercritical conditions [14,15]. Among others, one reason accounting for the deviation is that the classical D^2 -Law is established for large open systems ($L/D_0 \gg 1$, L is the system size), which is not always the case in laboratory conditions, while simulations are inevitably limited to finite-size systems. It may be noted that the term “open” system is not contradictory with the “finite-size” system. Here, the former means free outflow of vapor from the control volume while the latter indicates the system (concerning temperature/concentration) is confined with Dirichlet boundary conditions in a finite space (as shown in Fig. 1). Recently, the mesoscopic lattice Boltzmann (LB) method has been used more and more widely for studying evaporation dynamics [6,8,16–19], mainly due to its advantages of natural incorporation of micro/mesoscale physics, easy treatment of liquid-vapor interface, and highly efficient algorithm [20–23]. Ledesma-Aguilar *et al.* [16] applied a phase-field LB method to simulate sessile droplet evaporation, driven by a concentration gradient, by manipulating the order parameter at the boundary to induce a chemical potential gradient. Safari *et al.* [17,18] modeled droplet evaporation in open systems based on a phase-field LB method by adding a source term to the mass equation in order to account for phase change due to the temperature gradient or vapor concentration gradient. Li *et al.* [8] investigated the contact line pinning-depinning mechanism of an evaporating droplet on chemically patterned surfaces based on the pseudopotential LB method, where the evaporation is driven by the temperature field via the nonideal equation of state. In addition, the LB method has been applied to various evaporation phenomena, such as the self-propelled motion of Leidenfrost droplets on ratchet surfaces [24], the evaporation induced by pressure variations (cavitation) [19],

drying of porous media [25], three-dimensional (3D) nanoparticle deposition by drying of colloidal suspension [6,7] and contact line dynamics of droplets evaporating on microribs [9]. A linear decrease of D^2 with t has been observed in many LB simulations [24–29], hence claiming the models to be validated against the classical D^2 -Law, although the slope was not compared with the evaporation constant K . By substituting the thermophysical properties into its definition, it was found that the evaporation constant K predicted by the above-mentioned LB simulations was smaller than its theoretical value. One cause for this underestimation is the use of 2D simulations, as the heating of a 2D droplet (liquid cylinder) is slower than heating a 3D droplet for which the classical D^2 -Law is established. In addition, the employed closed boundary condition (e.g., the periodic boundary or bounce-back scheme for the velocity field [25,27,28]) and small density ratio (e.g., order of 10) may also have some effects. Also, it was reported by Albernaz *et al.* [30] that the decrease of D^2 with t was not perfectly linear in 2D LB simulations.

As discussed above, the classical D^2 -Law is established for large 3D systems, while a finite size and/or 2D system is encountered in many situations, which has not yet been systematically investigated. In experiments, examples of finite-size systems are the evaporation of a single droplet in microfluidic systems [13,31] or a dense collection of millimetric/micrometric droplets in a macroscale combustion chamber [32]. From the numerical simulation point of view, the system size is always limited by the computational cost [14], and 2D simulations are often considered for preliminary studies or model validation [29]. To clarify the above issues, the present work presents a revised analysis of single droplet evaporation in open systems, taking into consideration the two effects (finite size and 2D). Considering the rapidly increased use of the mesoscopic LB method in the modeling of evaporation phenomena, we will explore how to consistently simulate single component droplet evaporation by this method, with an emphasis on the proper boundary conditions treatment. LB simulation results for different boundary schemes, in 2D and 3D ($d = 2$ and 3), are compared with the classical D^2 -Law, and the present analysis. Besides, the distribution of the temperature field, which is rarely discussed in the literature, will also be analyzed and investigated.

The paper is organized as follows. The theoretical analysis is given in Sec. II. Section III briefly introduces the LB method and the implementation of the boundary conditions. Section IV presents the simulation results, comparisons, and discussions. Finally, concluding remarks are given in Sec. V.

II. THEORETICAL ANALYSIS

As sketched in Fig. 1(a), a static droplet evaporates due to the temperature difference between the boundary and the droplet surface, i.e., $\Delta T = T_2 - T_s$. The theoretical solution can be obtained based on the following assumptions: (i) the evaporation process is quasisteady, (ii) the viscous heat dissipation and the buoyancy force are negligible, (iii) the thermophysical properties (λ and c_p) are constant, and (iv) the temperature inside the droplet is uniform and maintained at the surface temperature T_s , equal to the temperature at vapor saturation. Assumption (iv) works well when the evaporation

process is slow and quasistatic, and thus the heat transferred from the vapor into the droplet is balanced by the liquid-vapor latent heat [1,10]. With assumptions (i) and (ii), the governing equation of heat transport in spherical coordinates can be simplified as

$$\rho c_p v_r \frac{\partial T}{\partial r} = \frac{1}{r^2} \frac{\partial}{\partial r} \left(\lambda r^2 \frac{\partial T}{\partial r} \right), \quad r \geq r_s, \quad (3)$$

where v_r is the velocity component in the radial direction and $r_s = D/2$ is the radius of the droplet. According to assumptions (iii) and (iv), the energy balance at the droplet surface is

$$\lambda \frac{\partial T}{\partial r} \Big|_{r=r_s} = \rho_s v_{r,s} h_{fg}, \quad (4)$$

where h_{fg} is the latent heat of vaporization, ρ_s and $v_{r,s}$ are the density and radial velocity at the droplet surface (indicated by the index s). Using the continuity condition ($r^2 \rho v_r = r_s^2 \rho_s v_{r,s}$) and Eq. (4), and integrating Eq. (3) from r_s to r , we obtain

$$r_s^2 \rho_s v_{r,s} [c_p(T - T_s) + h_{fg}] = r^2 \lambda \frac{\partial T}{\partial r}. \quad (5)$$

Separating the variables and integrating Eq. (5) from the droplet surface to the boundary gives

$$r_s^2 \rho_s v_{r,s} c_p \left(\frac{1}{r_s} - \frac{1}{r_2} \right) = \lambda \ln(1 + B), \quad (6)$$

with $B = c_p(T_2 - T_s)/h_{fg}$. Substituting the continuity condition within the droplet ($\rho_s v_{r,s} = -\rho_l \partial r_s / \partial t$) and separating the variables, Eq. (6) is rewritten as

$$d \left[r_s^2 \left(\frac{1}{2} - \frac{r_s}{3r_2} \right) \right] = -\frac{\lambda}{\rho_l c_p} \ln(1 + B) dt. \quad (7)$$

Integrating the above equation over time, the time evolution of D is obtained as

$$\left(1 - \frac{2D}{3L} \right) D^2 = \left(1 - \frac{2D_0}{3L} \right) D_0^2 - Kt, \quad (8)$$

where $K = 8\lambda/(\rho_l c_p) \ln(1 + B)$. It is seen from Eq. (8) that, for finite-size systems, the decrease of D^2 with t depends on the size L and does not follow the classical D^2 -Law as given in Eq. (1).

The temperature field can also be obtained at a given time ($D = 2r_s$ is fixed), by defining the index $\xi_{3D} = \ln(1 + B)/(1 - D/L)$ and substituting it into Eq. (5), which gives

$$\xi_{3D} \frac{r_s}{r^2} dr = \frac{dT}{(T - T_s + h_{fg}/c_p)}. \quad (9)$$

Integrating Eq. (9) from r_s to r , we finally get

$$T = \frac{h_{fg}}{c_p} \left\{ \exp \left[\xi_{3D} \left(1 - \frac{r_s}{r} \right) \right] - 1 \right\} + T_s, \quad r \geq r_s. \quad (10)$$

The temperature distribution outside the droplet shows an exponential profile.

For the 2D situation ($d = 2$), similar derivations [see Eqs. (A1)–(A6) in Appendix A] based on the energy transport equation in the cylindrical coordinates can be conducted to get the theoretical solution of D and T . The time evolution of D is

then expressed as follows:

$$[\ln(L/D) + 1/2]D^2 = [\ln(L/D_0) + 1/2]D_0^2 - Kt, \quad (11)$$

which is consistent with the analysis in Ref. [30]. Analogously, introducing the index $\xi_{2D} = \ln(1 + B)/\ln(L/D)$, the temperature field is given as

$$T = \frac{h_{fg}}{c_p} \left[\left(\frac{r}{r_s} \right)^{\xi_{2D}} - 1 \right] + T_s, \quad r \geq r_s, \quad (12)$$

which indicates a power-law distribution of the temperature field outside a 2D evaporating droplet.

From the above analysis, we observe that, for droplet evaporation in finite-size open systems, the decrease of D^2 with t depends on both the evaporation constant K and the system size ratio L/D_0 , and the spatial dimension d , yielding a deviation from the classical D^2 -Law. For the 3D system ($d = 3$), the D^2 - t evolution [Eq. (8)] approaches the classical D^2 -Law asymptotically with increasing system size and finally converges when $L/D_0 \gg 1$. In contrast, for the 2D system ($d = 2$), it is hard to get convergent solutions by simply increasing L . For the isothermal two-component counterpart, as illustrated in Fig. 1(b), the solutions of diameter evolution and concentration profile are essentially equivalent to the single-component droplet evaporation driven by the temperature gradient [see Eqs. (B6) and (B8)–(B10) in Appendix B], and we will not go into further detail.

III. NUMERICAL MODEL

A. Hybrid pseudopotential CLBM

The LB method can be viewed as a mesoscopic ‘‘computational fluid dynamics’’ approach that simulates complex fluids by solving a specific discrete Boltzmann equation for the density distribution function (DDF) f_i [20,33–40]. A standard LB algorithm consists of two steps: (i) the collision step, representing the time relaxation towards the local equilibrium state due to molecular collisions, and (ii) the streaming step, standing for molecular free streaming. The streaming step is independent of the collision models, which streams the postcollision DDF (f_i^*) at space-time point (\mathbf{x}, t) to the neighboring lattice point along the direction of the discrete velocity \mathbf{e}_i within a time step Δt , i.e.,

$$f_i(\mathbf{x} + \mathbf{e}_i \Delta t, t + \Delta t) = f_i^*(\mathbf{x}, t). \quad (13)$$

The hydrodynamic variables (density ρ and velocity \mathbf{u}) are updated after the streaming step by the following definitions:

$$\rho = \sum_i f_i, \quad \rho \mathbf{u} = \sum_i f_i \mathbf{e}_i + \Delta t \mathbf{F}/2, \quad (14)$$

where \mathbf{F} is the total force exerted on the fluid.

Various collision models can be chosen to suit the problems under investigation, which have been reviewed in detail and can be integrated into a unified framework [21]. In the present work, we use the cascaded collision model [41], which possesses very good numerical stability and therefore helps to conduct simulations at large liquid-vapor density ratios. In the cascaded lattice Boltzmann model (CLBM), the DDF is first projected onto the central moment space, then the central moments of different orders are relaxed separately,

and finally, the postcollision DDF is reconstructed. To make the implementation more efficient, the collision step can be described as follows [42,43]:

$$f_i^*(\mathbf{x}, t) = f_i(\mathbf{x}, t) - (\mathbf{M}^{-1}\mathbf{N}^{-1}\mathbf{S}\mathbf{N}\mathbf{M})[f_i(\mathbf{x}, t) - f_i^{eq}(\mathbf{x}, t)] + \Delta t \mathbf{M}^{-1}\mathbf{N}^{-1}(\mathbf{I} - \mathbf{S}/2)\mathbf{N}\mathbf{M}\mathbf{R}_i, \quad (15)$$

where f_i^{eq} is the equilibrium DDF, \mathbf{M} is a transformation matrix, \mathbf{N} is a lower triangular shift matrix, \mathbf{I} is the unit matrix, \mathbf{S} is a (block) diagonal relaxation matrix, and R_i represents the forcing term in the discrete velocity space. The explicit formulations of \mathbf{M} , \mathbf{N} and their inverses depend on the discrete velocity model and the adopted central moments set. In this work, we use a set of natural central moments originally proposed in Ref. [43], which gives very concise and sparse expressions for \mathbf{M} and \mathbf{N} . Besides the computational efficiency, such a central-moment set possesses an excellent portability across different lattices/dimensions [43,44]. For example, a 2D model can be directly obtained from a 3D model by extracting a subset of the 3D central moments and the corresponding rows and columns in \mathbf{M} and \mathbf{N} , which makes it very convenient in the following simulations with different spatial dimensions.

To simulate multiphase flows, four main types of multiphase LB models have been developed: the color-gradient model [45,46], the pseudopotential model [47,48], the free-energy model [49,50], and the phase-field model [51]. For detailed descriptions of these models, interested readers are directed to the comprehensive review papers [20,22,23]. Among them, the phase-field and pseudopotential models have been widely used in evaporation simulations [20]. To simulate evaporation based on the phase-field model, a source term is usually added to the continuity or Cahn-Hilliard equation to define the evaporation rate [17,18,52], which implies the evaporation rate is an *input rather than output*. In contrast, the pseudopotential model has no such limitation: the liquid-vapor phase change can be driven by temperature deviation from equilibrium via the nonideal equation of state [8,24,25,53]. In this work, the pseudopotential model is adopted, where the fluid-fluid interaction force is mimicked by a pseudopotential-based interaction force [47,48]:

$$\mathbf{F} = -G\psi(\mathbf{x}) \sum_i w(|\mathbf{e}_i|^2) \psi(\mathbf{x} + \mathbf{e}_i \Delta t) \mathbf{e}_i, \quad (16)$$

where w is the weight, and the square-root form pseudopotential $\psi = \sqrt{2(p_{EOS} - \rho c_s^2)/Gc^2}$ is used [54], which incorporates the nonideal equation of state (EOS) p_{EOS} into the system. For such a choice, the interaction strength is fixed to be $G = -1$, and c and c_s are the lattice speed and sound speed, respectively. As discussed in Refs. [42,43], the interaction force \mathbf{F} can be consistently incorporated into the CLBM via the forcing term R_i .

The temperature governing equation for the liquid-vapor phase-change process can be written as [55],

$$\frac{\partial T}{\partial t} = -\mathbf{u} \cdot \nabla T + \frac{1}{\rho c_v} (\lambda \nabla^2 T + \nabla \lambda \cdot \nabla T) - \frac{T}{\rho c_v} \left(\frac{\partial p_{EOS}}{\partial T} \right)_{\rho} \nabla \cdot \mathbf{u}. \quad (17)$$

In the evaporation simulations, the multiphase flow field is solved by the pseudopotential CLBM [Eqs. (15) and (16)], while the temperature field [Eq. (17)] is solved by the finite difference method. The second-order Runge-Kutta scheme and the isotropic central scheme are used for the time marching and spatial discretization, respectively. The flow and temperature fields are coupled via a nonideal Peng-Robinson EOS [54],

$$p_{EOS} = \frac{\rho \bar{R} T}{1 - b\rho} - \frac{a\varphi(T)\rho^2}{1 + 2b\rho - b^2\rho^2}, \quad (18)$$

where $\bar{R} = 1$ is the gas constant, and $\varphi(T) = [1 + (0.37464 + 1.54226\varpi - 0.26992\varpi^2)(1 - \sqrt{T/T_c})]^2$, with the acentric factor $\varpi = 0.344$ in this work. The critical pressure p_c and temperature T_c are determined by $a = 0.4572R^2T_c^2/p_c$ and $b = 0.0778RT_c/p_c$. Consistent with the analysis by Li *et al.* [56], the interface thickness W is approximately proportional to $1/\sqrt{a}$. When the reduced temperature $T_r = T/T_c$ is given, the saturated liquid density ρ_l^{sat} and vapor density ρ_v^{sat} can be obtained using Eq. (18) based on the Maxwell construction. Two density ratios are considered in this work: (i) $\rho_r = \rho_l^{\text{sat}}/\rho_v^{\text{sat}} \approx 71$ ($a = 1/45$, $b = 2/21$, $T_r = 0.75$, with $W \approx 3.6$) and (ii) $\rho_r \approx 328$ ($a = 1/125$, $b = 2/21$, $T_r = 0.65$, with $W \approx 4.6$). The saturated coexistence densities can be correctly reproduced by the mechanical stability adjustment method developed by Li *et al.* [56,57]. The hybrid formulation was subsequently extended to CLBM and systematically verified [53,58]. Moreover, it was shown that the resulting hybrid multiphase CLBM had superior stability and was able to simulate large-scale pool boiling [53] and forced-convection boiling [58] systems covering the complete boiling curve and typical boiling regimes. In this study, the treatments proposed by Saito *et al.* [58] and Fei *et al.* [53] are combined and adopted for both 2D and 3D simulations. Using the Chapman-Enskog analysis, the following macroscopic equations can be recovered:

$$\partial_t \rho + \nabla \cdot (\rho \mathbf{u}) = 0,$$

$$\begin{aligned} \partial_t (\rho \mathbf{u}) + \nabla \cdot (\rho \mathbf{u} \mathbf{u}) &= -\nabla (\rho c_s^2) + \nabla \cdot [\rho \nu (\nabla \mathbf{u} + (\nabla \mathbf{u})^T) \\ &\quad + \rho (\nu_b - 2\nu/d) (\nabla \cdot \mathbf{u}) \mathbf{I}] \\ &\quad + \mathbf{F} - 2G^2 c^4 \sigma \nabla \cdot (|\nabla \psi|^2 \mathbf{I}), \end{aligned} \quad (19)$$

where ν and ν_b are the kinetic and bulk viscosities, respectively, and the last term is the additional tuning term. The tuning parameter is chosen as $\sigma = 0.109$ and 0.113 for the case with $\rho_r = 71$ and 328 , respectively. By absorbing the last term into the pressure tensor, the mechanical stability condition can be adjusted so that the liquid-vapor coexistence densities are consistent with the Maxwell construction.

B. Shrinkage effect

Like other diffuse-interface numerical models, the adopted LB model also suffers from shrinkage effects, meaning that droplets below a critical size shrink spontaneously due to the redistribution of interface and bulk energies to minimize the system energy [59–61]. The critical size D^* is defined as the

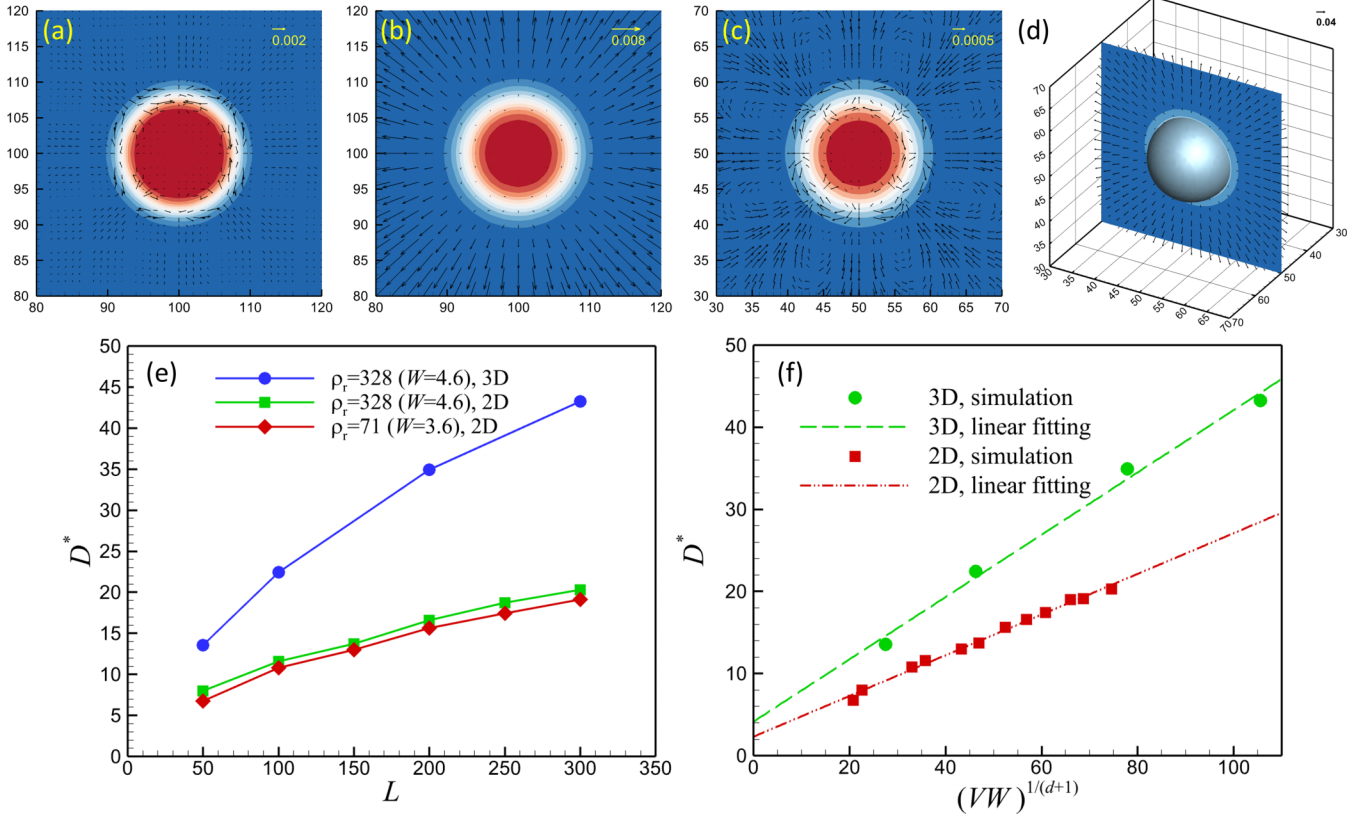


FIG. 2. Illustration of the shrinkage effect. (a)–(d) An initial droplet with $D_0 = 16$ in four configurations, i.e., ($L = 200$, $W = 3.6$, 2D), ($L = 200$, $W = 4.6$, 2D), ($L = 100$, $W = 4.6$, 2D), and ($L = 100$, $W = 4.6$, 3D), respectively. The maximum magnitude of the velocity field is indicated by the reference vector. (e) The critical droplet size D^* changes with domain size L . (f) D^* changes with $(VW)^{1/(d+1)}$, where W is the interface thickness, V is the system volume, and d is the spatial dimension.

size when shrinkage starts to take place and depends on the system size L , interface thickness W for suspending droplets [59,60], and also on the contact angle for sessile droplets [61]. Such a shrinkage effect needs to be carefully addressed in the present investigation. Therefore, the critical droplet size D^* is first determined iteratively by changing D_0 in small steps for each case until the limit between stable and shrinking was attained.

Figures 2(a)–2(d) shows the density contours and velocity field of a droplet initialized in various computational configurations. Although the initial droplet size is the same ($D_0 = 16$), the behavior in each case is quite different. The droplet in case (a) shows a sharp interface and remains stable, i.e., $D^* < 16$. When the interface thickness W is increased, spontaneous “evaporation” occurs in the isothermal case, as demonstrated by the radial velocity field in case (b), i.e., $D^* > 16$. Fixing the thickness W while decreasing the system size L , the droplet becomes stable again, therefore we have $D^* < 16$ in case (c). With the same interface thickness and system size used in 3D, the droplet becomes unstable again, i.e., $D^* > 16$, as shown in (d). It may be noticed that the eight symmetric vortices in cases (a) and (c) are due to the spurious velocity, whose magnitude is on the order of $O(10^{-3})$ and $O(10^{-4})$ for thinner and thicker interface cases, respectively. The above results show that the critical diameter depends on the interface thickness W , system size L and spatial dimension

d in the present numerical model. It is further demonstrated in Fig. 2(e) that D^* increases with L , and varies with W and d at a given L . As analyzed in the literature, the critical diameter scales as $D^* \propto (VW)^{1/3}$ in 2D [59,60] and $D^* \propto (VW)^{1/4}$ in 3D [59,61], with V being the system volume, which is also confirmed by our results [seen in Fig. 2(f)].

Actually, the shrinkage effect can be regarded as an inherent feature in the diffuse-interface numerical models due to the nonzero interface thickness. To our knowledge, the effects of interface thickness were not considered in the previous LB simulations of droplet evaporation, which may have led to less reliable results of the predicted droplet diameter in the late stage (droplet smaller than D^*). To avoid this effect, the evaporation simulations are stopped when the droplet size is smaller than D^* , in the remaining simulations.

C. Boundary conditions

As sketched in Fig. 1(a), the evaporating droplet is subjected to a Dirichlet boundary for the temperature field, which is straightforward to implement by imposing a constant boundary temperature T_2 in the simulation. However, additional treatment (boundary scheme) is required to obtain the unknown density distribution functions streaming from the outside of the boundary. It is noted that different boundary conditions have been used in evaporation simulations, such

as the periodic boundary condition as in Ref [27,28,53], the nonslip boundary condition in Ref. [25], and the (constant) pressure boundary condition in Refs. [26,29]. Correspondingly, different boundary schemes have been employed to obtain the unknown density distribution functions, including the heuristic periodic scheme and bounce-back scheme, the nonequilibrium bounce-back (or Zou-He) scheme [62], and the nonequilibrium extrapolation scheme [63].

However, there is still no analysis about whether these boundary schemes are consistent with the “open system” considered in Fig. 1. In this subsection, the previously adopted boundary schemes are summarized and an alternative boundary scheme is proposed, which will be compared in the following simulations.

Periodic scheme: The periodic scheme assumes the flow is spatially periodic (with a spatial period L). Therefore, the incoming (unknown) distribution functions on one boundary are set to be the streaming out (known) distribution functions on the opposite boundary.

Bounce-Back scheme: The bounce-back scheme assumes the boundary is a solid wall, such that the postcollision density distribution function hits the boundary (i.e., streams in a direction to leave system) and reverses its direction as $f_i(\mathbf{x}_b, t + \Delta t) = f_i^*(\mathbf{x}_b, t)$, where $\mathbf{e}_i = -\mathbf{e}_i$ is the discrete velocity whose density distribution function is unknown at the boundary node \mathbf{x}_b .

Zou-He scheme: Zou-He scheme is constructed based on the definition of the macroscopic fluid variables [Eq. (14)] and the supplementary condition, i.e., the bounce-back rule for the nonequilibrium part of specific density distribution functions (e.g., for the 2D case at the bottom boundary, $f_2 - f_2^{eq} = f_4 - f_4^{eq}$). For the evaporation simulation, if the pressure at the boundary node is specified as the saturated vapor pressure p_v^{sat} , the boundary density ρ_b can be calculated by the EOS with the boundary temperature T_2 [30], i.e., $p_{EOS}(\rho_b, T_2) = p_v^{\text{sat}}$. In addition, it is implicitly assumed that the velocity is normal to the boundary (zero tangential velocity component) [62].

Nonequilibrium extrapolation scheme: In this scheme, the unknown distribution function is decomposed into its equilibrium and nonequilibrium parts, where the equilibrium part

is constructed based on the macroscopic variables, while the nonequilibrium part is approximated by extrapolation [63]. For the present case, we have $f_i^{\text{eq}}(\mathbf{x}_b, t + \Delta t) = f_i^{\text{eq}}(\rho_b, \mathbf{u}_f) + (f_i - f_i^{\text{eq}})|_{(\mathbf{x}_f, t + \Delta t)}$, where \mathbf{u}_f is the updated velocity at the neighboring node $\mathbf{x}_f = \mathbf{x}_b + \mathbf{e}_i \Delta t$ and the boundary density ρ_b is obtained in the same way as the Zou-He scheme.

Modified nonequilibrium extrapolation scheme: From the definitions of the periodic scheme and bounce-back scheme, it is noted that both schemes correspond to a closed system because the system mass is conserved, and thus incompatible with droplet evaporation in open systems. In contrast, the Zou-He scheme and nonequilibrium extrapolation scheme allow the outflow of the vapor from the system, which is consistent with the configuration in Fig. 1(a) to some extent. However, they still suffer from the constant pressure boundary hypothesis, which is contradictory to our considered situation. As the droplet size decreases due to evaporation, both the pressure inside and outside of the droplet will increase according to Laplace’s equation [64], i.e., $p_j = p_j^{\text{sat}} + [\rho_j^{\text{sat}}/(\rho_l^{\text{sat}} - \rho_g^{\text{sat}})]\kappa\gamma$, where γ is the surface tension, κ is the mean curvature ($\kappa = 1/R$ in 2D or $2/R$ in 3D), and $j = l, v$ corresponds to liquid or vapor, respectively. For a large droplet ($R \rightarrow \infty$), the saturated pressure is recovered in both the liquid and vapor phases. In the simulations, imposing the saturated pressure (density) for the droplet with the initial size R_0 , it is observed that the normalized vapor pressure increases during the evaporation process (decreasing radius), especially for larger density ratio or spatial dimension (2D vs 3D) [seen in Fig. 3(a)]. Therefore, such adaptive vapor pressure depending on droplet radius should be implemented in the boundary scheme. Compared with the Zou-He scheme, the nonequilibrium extrapolation scheme is more suitable for the present problem because the boundary velocity is extrapolated from the inner nodes, free from the zero tangential velocity assumption in Zou-He. To incorporate such an effect, the nonequilibrium extrapolation scheme can be modified as $f_i^{\text{eq}}(\mathbf{x}_b, t + \Delta t) = f_i^{\text{eq}}(\rho_v, \mathbf{u}_f) + (f_i - f_i^{\text{eq}})|_{(\mathbf{x}_f, t + \Delta t)}$, where the boundary vapor density ρ_v is calculated according to $p_{EOS}(\rho_v, T_2) = p_v(R)$. For a given temperature difference $\Delta T = T_2 - T_s$, ρ_v also changes

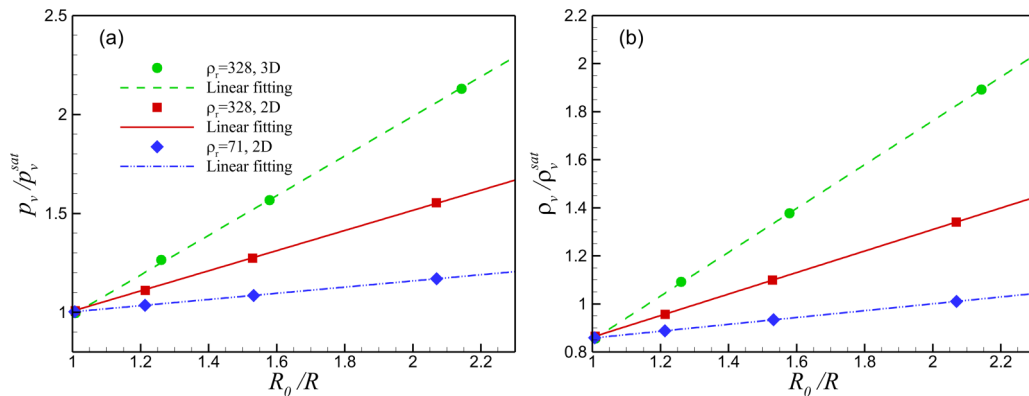


FIG. 3. (a) Change of normalized vapor pressure at the saturated temperature with droplet size. (b) Change of normalized vapor density, obtained according to $p_{EOS}(\rho_v, T_2) = p_v(R)$, with droplet size. Three different cases are considered at the fixed normalized temperature difference $\Delta T = T_2 - T_s = 0.1T_c$.

TABLE I. Numerical setup. All the variables are given in lattice units (L.U).

Configurations	Case number	λ	C_p	$\Delta T/T_c$	B	K
2D, $\rho_r = 71, D_0 = 60\Delta x$	1	40	800	0.25	30.58	0.1799
	2	20	400	0.2	12.23	0.1345
	3	10	200	0.2	6.12	0.1022
	4	10	200	0.1	3.06	0.0730
	5	4	100	0.1	1.53	0.0387
2D, $\rho_r = 328, D_0 = 60\Delta x$	6	2	200	0.1	2.72	0.0125
	7	1.5	200	0.1	2.72	0.0094
	8	1.0	200	0.1	2.72	0.0062
	9	0.5	200	0.1	2.72	0.0031
3D, $\rho_r = 328, D_0 = 70\Delta x$	10	2	200	0.1	2.72	0.0125
	11	1	100	0.1	1.36	0.0082
	12	1	200	0.1	2.72	0.0062

linearly with $1/R$, as shown in Fig. 3(b). In the following simulations, the original nonequilibrium extrapolation scheme, where the boundary pressure is fixed at the saturated pressure p_v^{sat} , is marked as *Nonequilibrium1*, and the modified version with the adaptive boundary pressure $p_v(R)$ is denoted by *Nonequilibrium2*.

IV. RESULTS AND DISCUSSION

In this section, droplet evaporation simulations are carried out in different configurations, including 2D and 3D, at both moderate ($\rho_r = 71$) and large ($\rho_r = 328$) density ratios. A square and cubic computational domains are used to mimic the 2D and 3D systems, respectively. Unless otherwise specified, the system size is set as $L = 200\Delta x$ (Δx is the lattice spacing). The initial droplet size is slightly larger in 3D because a 3D droplet suffers from a larger critical size than a 2D droplet under the same condition, as shown in Fig. 2(f). By changing the thermal conductivity λ , the specific heat capacity c_p , and the temperature difference ΔT , the Spalding number B , and the evaporation constant K can span over a wide range. The parameters used in lattice units are given in Table I. The lattice units can be converted to physical units based on the corresponding characteristic variables, as summarized in Appendix C. The phase-change latent heat is obtained using the standard numerical integration method based on the EOS [53,58]. Our parameter choice leads to $h_{fg} = 0.2597$ and $h_{fg} = 0.1049$ for the two density ratios $\rho_r = 71$ and $\rho_r = 328$, respectively.

A. Effects of boundary schemes

First, the effect of the different boundary schemes is tested based on simulations of Case 1. The snapshots of the droplet evaporation at $t = 10000\Delta t$ are shown in Fig. 4, showing vector velocity and isoline temperature fields. For the periodic scheme and bounce-back scheme, the velocity is constrained to the impermeable condition at the boundary, which conserves the total mass in the system as shown in Figs. 4(a) and 4(b), where the latter also suffers from the nonslip condition [Fig. 4(b)]. As a result, the vapor cannot escape from the system, which in turn heats up the droplet more significantly and breaks down the isothermal assumption inside the droplet,

as shown by temperature contours inside the droplet. For the other three schemes, the vapor generated at the droplet surface can flow out of the system and the temperature within the droplet is kept almost uniform, as seen in Figs. 4(c)–4(e). In comparison with the Zou-He boundary scheme [Fig. 4(c)], the velocity field predicted by the nonequilibrium extrapolation schemes [Figs. 4(d) and 4(e)] is more reasonable, because the radial velocity vectors are consistent with the axisymmetric evaporation condition.

The time evolution of D^2 predicted by the present LB model for different boundary schemes is shown in Fig. 5(a), allowing comparison with the classical D^2 -Law and the revised theoretical solution in Eq. (11). The D^2 evolutions predicted by the model with the periodic and bounce-back schemes are quite similar to each other, despite the slight difference in the velocity field mentioned above, and significantly underestimate the evaporation rate. Although the D^2 - t profiles can be approximately linearly fitted, as done in previous work [24–29,53], it is clearly not a sufficient validation of the classical D^2 -Law due to the significant difference between model results and the classical D^2 -Law. As for the Zou-He and two nonequilibrium extrapolation schemes, the predictions are in close agreement with the theoretical solutions, mainly due to the “open boundary” feature as discussed before. Among them, *Nonequilibrium2* gives the most accurate solution, especially for the end-stage due to the introduction of an adaptive pressure boundary. We note that classical D^2 -Law deviates strongly from the theoretical solution in these 2D cases. The reduced temperature profiles for the different boundary schemes, when half of the droplet is evaporated ($V/V_0 \approx 0.5$), are shown in Fig. 5(b). Consistent with the temperature fields shown in Figs. 4(a) and 4(b), the periodic and bounce-back schemes lead to much higher temperature predictions than the theoretical solution [Eq. (12)] in the vapor phase [$x < (L-D)/2$], and therefore the temperature in the droplet is nonconstant. The other three schemes give better predictions and almost keep a constant temperature within the droplet, among which *Nonequilibrium2* predicts the most accurate results. For both the predicted droplet diameter and temperature field, *Nonequilibrium1* and *Nonequilibrium2* outperform the other boundary schemes and will be used in the remainder of the work.

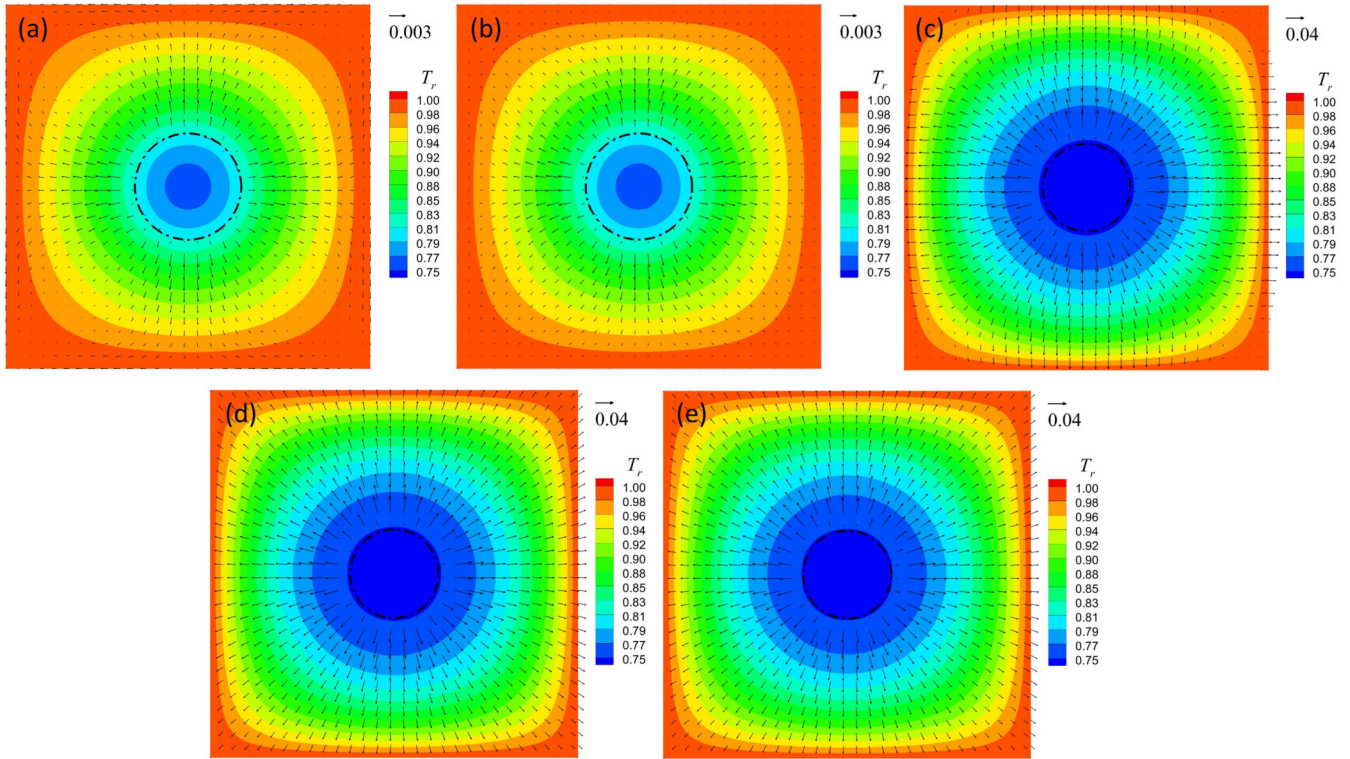


FIG. 4. Reduced temperature ($T_r = T/T_c$) distributions and velocity vectors of Case 1 for different boundary schemes: (a)–(e) correspond to *Periodic*, *Bounce-back*, *Zou-He*, *Nonequilibrium1*, and *Nonequilibrium2* schemes, respectively. The dashed-dotted circle indicates the location of the liquid-vapor interface.

B. 2D droplet evaporation

Figure 6 shows, for Cases 2–9, the time evolution of D^2 for 2D droplet evaporation as predicted by the classical D^2 -Law, the theoretical solution [Eq. (11)], and the numerical results with the *Nonequilibrium1* and *Nonequilibrium2* boundary schemes. At moderate density ratio ($\rho_r = 71$), *Nonequilibrium1* agrees with the theoretical solution in the beginning, and deviates gradually with time, as seen in the first row (Cases 2–5). At a larger density ratio ($\rho_r = 328$, the second row), the results by *Nonequilibrium1* depart even more from the theoretical solutions. Such a trend is attributed to the

fact that the larger the density ratio, the more remarkable the change in vapor pressure (density) with droplet radius (as seen in Fig. 3), and therefore the more significant the deviations predicted by a constant pressure boundary condition (*Nonequilibrium1*). For both density ratios, the simulation results using the *Nonequilibrium2* scheme are in very good agreement with the theoretical solution, which further confirms the necessity to introduce an adaptive vapor pressure boundary. With decreasing evaporation constant K (from Cases 2 to 9), the total evaporation time (or droplet lifetime) increases successively. Moreover, it is observed that the D^2 - t

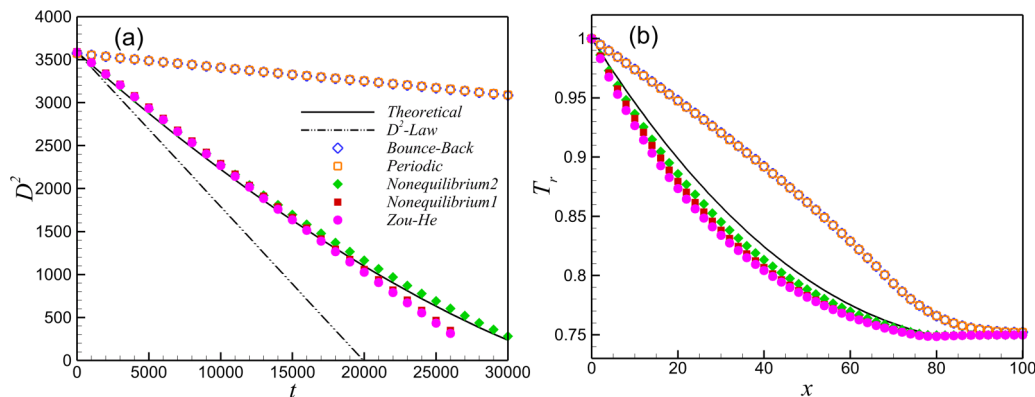


FIG. 5. Comparison between different boundary schemes for Case 1. (a) Change of D^2 with t ; (b) reduced temperature profile along the horizontal central line ($y = L/2$) at $V/V_0 \approx 0.5$.

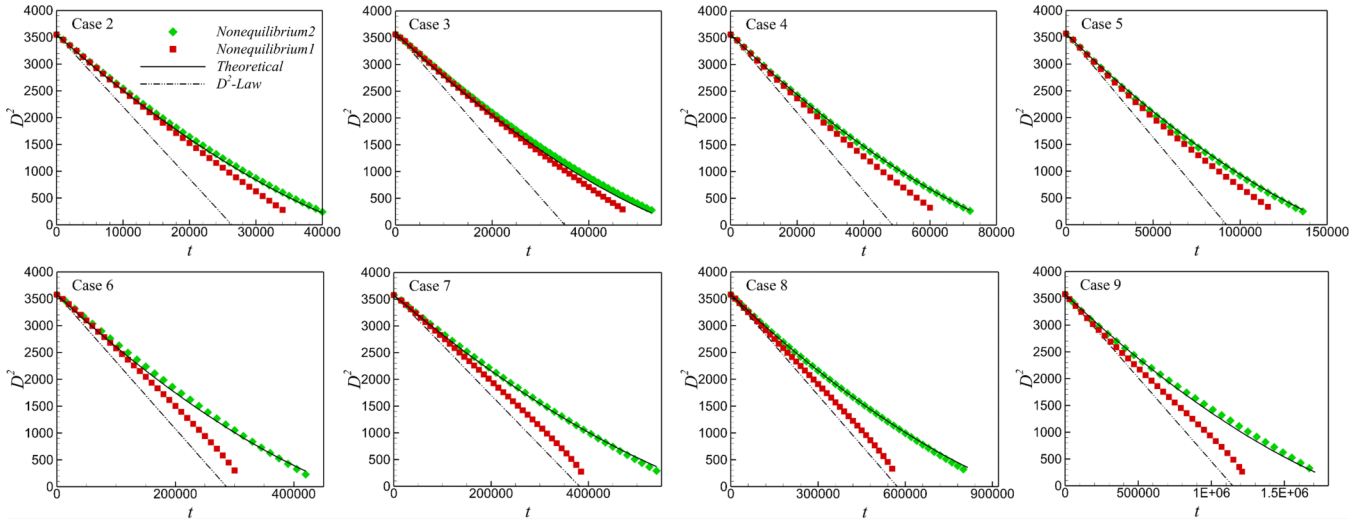


FIG. 6. Comparison of the time evolution of D^2 for 2D droplet evaporation between classical D^2 -Law, theoretical solution [Eq. (11)], and numerical results with *Nonequilibrium1* and *Nonequilibrium2* boundary schemes.

profiles are not necessarily linear, and the comparisons indicate an overestimation of the evaporation rate by the classical D^2 -Law in all considered cases.

At a given evaporated volume (V/V_0 is fixed), the temperature profile depends only on B and L , parameters that enter in index ξ_{2D} described in Eq. (12), therefore Cases 6–9 (with the same B) are identical and only Case 6 is presented. In Fig. 7, the temperature profiles at $V/V_0 \approx 0.5$ for Cases 2–6 are presented in graphs (a)–(e) respectively, with an additional graph (f) showing Case 6 at $V/V_0 \approx 0.3$. The theoretical temperature profiles, according to Eq. (12), are concave for

cases (a) and (b), approximately linear for cases (c) and (e), and convex for cases (d) and (f), when $\xi_{2D} > 1$, $\xi_{2D} \approx 1$ and $\xi_{2D} < 1$, respectively. Consistent with Fig. 6, for all the cases, *Nonequilibrium2* produces more accurate temperature solutions than *Nonequilibrium1*, and the deviations resulting from *Nonequilibrium1* are more significant at a larger density ratio. The temperature solved using *Nonequilibrium2* is always slightly lower than the one given by theory, which can be explained as a geometric effect: we use a square computational domain to mimic an axisymmetric system, with fixed boundary temperature, thus it is expected that the temperature

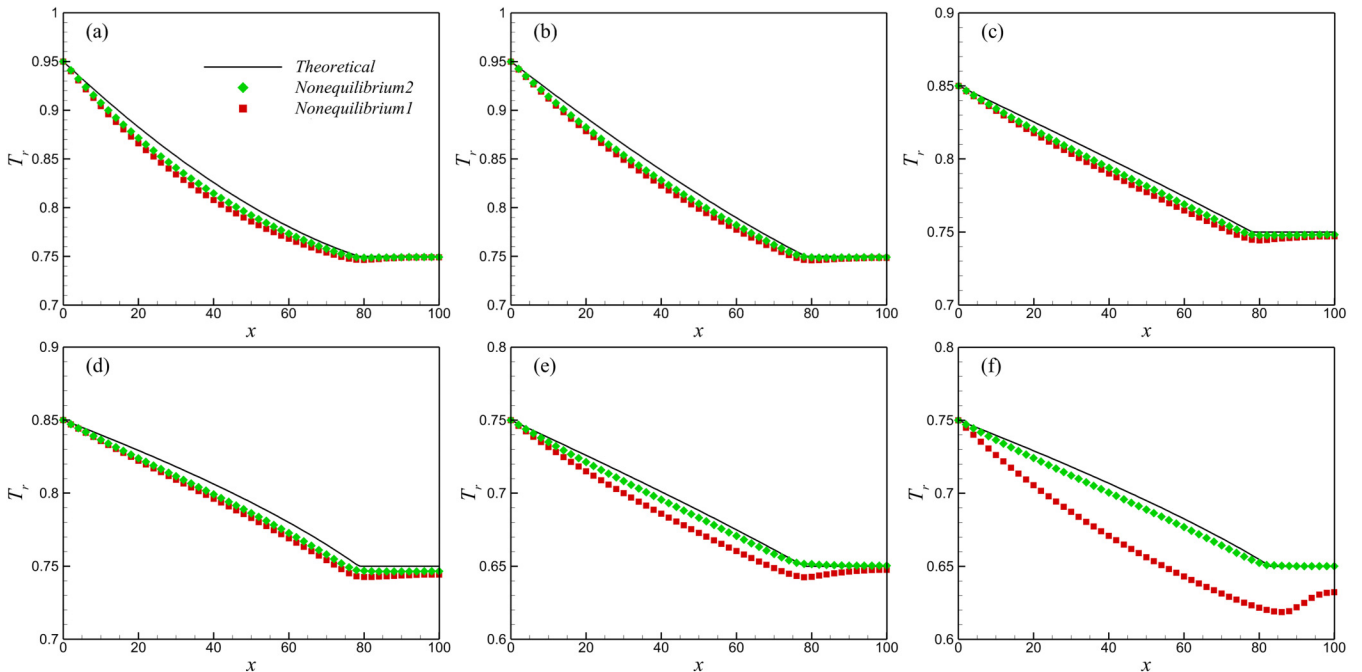


FIG. 7. Comparison between numerical results and theoretical solution [Eq. (12)] of temperature profiles for a 2D droplet evaporation. (a)–(e) are Cases 2–6 at $V/V_0 \approx 0.5$, respectively; (f) is Case 6 at $V/V_0 \approx 0.3$. The indexes in the theoretical solutions are $\xi_{2D} = 1.67, 1.28, 0.92, 0.60, 0.87,$ and 0.74 for (a)–(f), respectively.

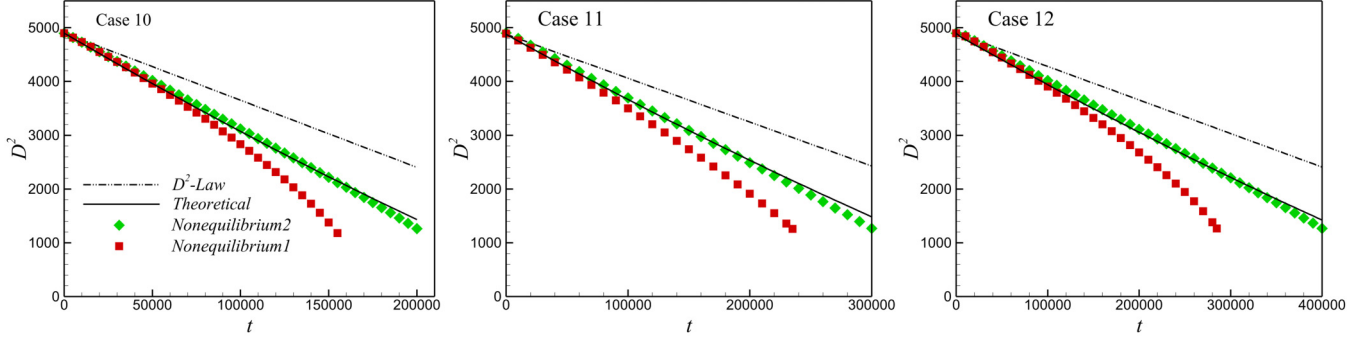


FIG. 8. Comparison of the time evolution of D^2 for a 3D droplet evaporation between classical D^2 -Law, theoretical solution [Eq. (8)], and numerical results with *Nonequilibrium1* and *Nonequilibrium2* boundary schemes.

decreases the fastest (and faster than the theory) along the horizontal/vertical center lines.

C. 3D droplet evaporation

We now address the 3D cases, and compare the D^2 evolution by D^2 -Law, our proposed theoretical equation, and simulations in Fig. 8. Different from the 2D cases, here we notice that simulations and theory predict faster evaporation rates than the classical D^2 -Law, which is intuitively explained by the more efficient heat transfer in 3D finite size systems. The evaporation simulated with *Nonequilibrium1* is too fast and departs from the theoretical solution after the initial state, e.g., $t > 50000\Delta t$ for Case 10, seen in Fig. 8(a). This observation is in line with those in Fig. 3 indicating a deficiency of using a constant pressure condition (*Nonequilibrium1*) for finite-size droplet evaporations, especially in 3D. In contrast, the prediction with an adaptive pressure condition (*Nonequilibrium2*) agrees well with theory on the whole, despite the slight differences at the late stage. The temperature profiles, as reported in Fig. 9 (Case 12 has the same ξ_{3D} as Case 10 and is not shown), show that the *Nonequilibrium2* results agree better with the theoretical solutions than *Nonequilibrium1*, consistent with the observation for D^2 in Fig. 8. In contrast with the 2D configuration, the temperature curve is always convex for different values of the index ξ_{3D} , because of the exponential distribution in Eq. (10). The deviations between

Nonequilibrium2 and the theory can also be explained with the geometric effects discussed above.

D. Error analysis

To analyze the errors between theory and numerical simulations, we calculate the relative errors in the droplet diameter E_D and temperature field E_θ as follows:

$$E_D = \frac{1}{t_{\text{end}}} \int_0^{t_{\text{end}}} \frac{(D - D_{\text{theory}})}{D_{\text{theory}}} dt,$$

$$E_\theta = \frac{1}{L} \int_0^L \frac{(\theta - \theta_{\text{theory}})}{\theta_{\text{theory}}} dx, \quad (20)$$

where $\theta = [(T - T_s)/\Delta T]|_{V/V_0=0.5}$ is the normalized temperature difference along the horizontal central line when the droplet is half evaporated. The average relative errors with standard deviations for simulations using *Nonequilibrium 1* and *2* are plotted in Fig. 10 for all the cases of Table I. Relative errors for temperature prediction are larger (in magnitude) and always negative as shown seen in Fig 10(b) compared to the diameter prediction in Fig. 10(a), mainly because the temperature decreases faster (from boundary to droplet surface) along the centerline direction than along diagonal direction for a square/cubic system. As also verifiable in Fig. 4, the temperature contours are slightly distorted outside the droplet, once more due to the geometric effect, and do not show an ideal axisymmetric (circular) shape. It should be noted

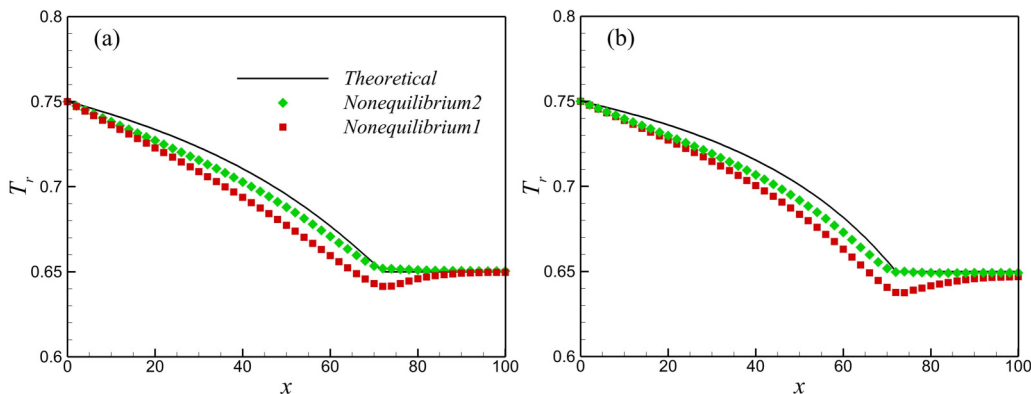


FIG. 9. Comparison between numerical results and theoretical solution [Eq. (10)] of temperature profiles for a 3D droplet evaporation at $V/V_0 \approx 0.5$. (a) Case 10; (b) Case 11.

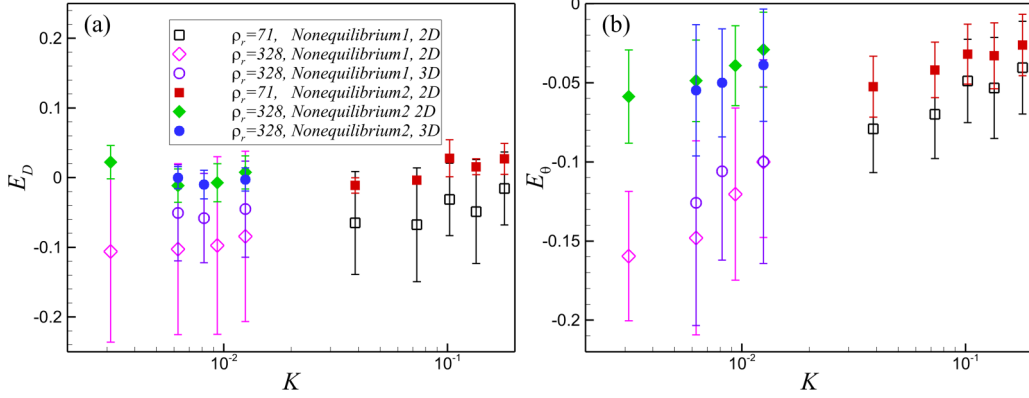


FIG. 10. Relative errors of the predicted droplet diameter (a) and temperature profile (b).

that using a square/cubic computational domain to model the cylinder/sphere system always introduces such small but inherent errors. For the constant pressure boundary condition (*Nonequilibrium1*), the average relative errors can be as large as 10% in droplet diameter and 15% in temperature. By using an adaptive pressure boundary condition (*Nonequilibrium2*), the relative errors are significantly reduced, by around five times and three times, for droplet diameter and temperature, respectively. The above results certainly confirm that an adaptive vapor pressure boundary should be adopted for droplet evaporation simulations in finite-size systems.

E. Effect of system size

We now discuss the effect of system size. To this aim, we perform a series of evaporation simulations in both 2D and 3D systems of different system sizes. Here, we only use the adaptive pressure boundary condition. The evaporation constant is fixed at $K = 0.0125$, corresponding to Case 6 and Case 10 in Table I. For both configurations, it is seen that the evaporation rate becomes slower with increasing system size L , and the simulation results agree well with the theoretical solutions, as shown in Fig. 11. For 2D configurations, most of the D^2 - t profiles are located above the D^2 -Law, except for the smallest system ($L = 120$). In contrast, the D^2 - t profiles always lie below the D^2 -Law for 3D configurations and tend to converge to the D^2 -Law for a very large system.

To interpret the mechanisms behind such observation, we determine the difference between the theoretical values for D^2 and those predicted by the classical D^2 -Law:

$$\begin{aligned}\Theta_{2D} &= (\varepsilon_{2D} - 1)D_0^2 + (1 - \delta_{2D})Kt, \\ \Theta_{3D} &= (\varepsilon_{3D} - 1)D_0^2 + (1 - \delta_{3D})Kt,\end{aligned}\quad (21)$$

where $\varepsilon_{2D} = [\ln(L/D_0) + 0.5]/[\ln(L/D) + 0.5]$, $\delta_{2D} = 1/[\ln(L/D) + 0.5]$, $\varepsilon_{3D} = (1 - 2D_0/3L)/(1 - 2D/3L)$ and $\delta_{3D} = 1/(1 - 2D/3L)$. The first term of Θ_{2D} is negative because $\varepsilon_{2D} < 1$. If $L/D > 1.65$, which is easily satisfied during most of the evaporation processes, we also have $\delta_{2D} < 1$. In such a case, the second positive term could cancel the first negative term, resulting in a positive Θ_{2D} . Therefore, the D^2 in most 2D cases is larger than that predicted by the D^2 -Law. An exception is for the initial evaporation stage in very small systems, where the second term can be negative ($\delta_{2D} > 1$) or positive but not large enough, so that $\Theta_{2D} < 0$ holds for a short time. Nevertheless, with evolving time, the second term increases and becomes sufficiently large enough to outperform the first term, explaining why the curve for the case $L = 120$ crosses the D^2 -Law profile in a later stage, shown in Fig. 11(a). For the 3D configuration, we always have $\varepsilon_{3D} < 1$ and $\delta_{3D} > 1$, giving $\Theta_{3D} < 0$. For large size limit ($L \rightarrow \infty$), we can obtain $\varepsilon_{3D} \rightarrow 1$ and $\delta_{3D} \rightarrow 1$, and therefore the result converges to the classical D^2 -Law with increasing L , as displayed in Fig. 11(b).

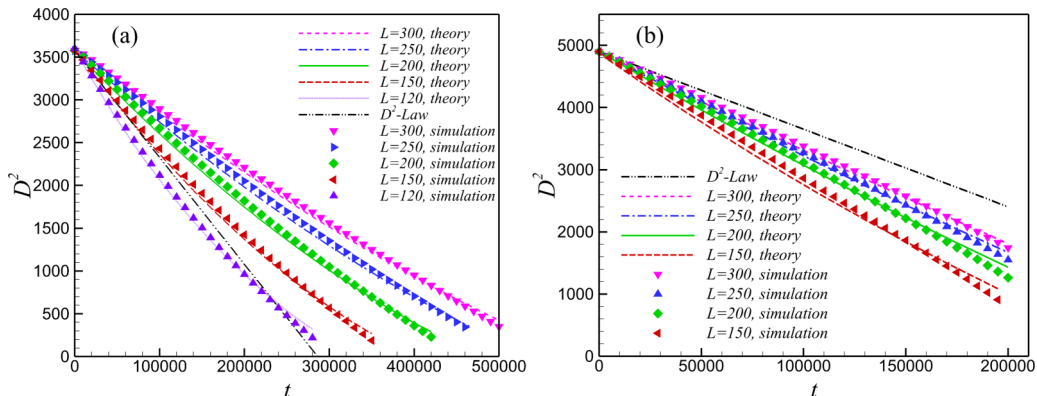


FIG. 11. Effect of the system size for single droplet evaporation with the evaporation constant $K = 0.0125$. (a) 2D configurations; (b) 3D configurations.

V. CONCLUDING REMARKS

In this work, single droplet evaporation in finite-size systems is investigated based on theoretical analysis and numerical simulations. The theoretical analysis starts from the governing equations of the energy transport in spherical (3D) and cylindrical coordinates (2D), under the assumptions of quasisteady evaporation with constant thermophysical properties and negligible viscous heat dissipation as well as buoyancy. The time evolution of the droplet diameter and the temperature distribution are obtained by integrating the simplified governing equations. The numerical simulations are conducted using a hybrid thermal multiphase cascaded lattice Boltzmann model, where the flow field and temperature field are solved by an improved cascaded lattice Boltzmann model and a finite difference solver, respectively. The two fields are naturally coupled via the Peng-Robinson equation of state. The following conclusions can be obtained from the study:

(1) Generally, the time evolution of D^2 for single droplet evaporation in finite size systems does not follow the classical D^2 -Law. For a 2D configuration, the D^2 - t relation is divergent when increasing the system size, while for a 3D configuration it is convergent to the D^2 -Law in the large system limit. The temperature profile outside the 2D evaporating droplet obeys a power-law distribution, whose concavity/convexity depends on the value of an index. In contrast, the temperature field in the 3D evaporation process follows an exponential distribution and is always convex.

(2) To correctly simulate droplet evaporation by a diffuse-interface model such as LBM, the shrinkage effect, i.e., the numerical loss of droplet mass, should be carefully considered. To avoid such a defect, a simple strategy is to stop the simulations when the droplet size reaches a critical size. It is further strongly suggested not to use the widely used periodic scheme and bounce back scheme in the boundary treatment. To reduce the errors introduced by using a constant vapor pressure boundary, an adaptive vapor pressure needs to be adopted, especially for large density ratio and/or 3D cases.

(3) By carefully designing the implementation of boundary conditions, single droplet evaporation in both 2D and 3D systems with density ratio up to 328 within a wide range of the evaporation constant ($K = [0.003, 0.18]$) is numerically reproduced. The simulation results agree well with the theoretical solutions for both the droplet diameter evolutions and the temperature distributions with the proposed adaptive vapor pressure boundary condition.

Although the present simulations are based on the lattice Boltzmann method, the proposed numerical treatments would provide general guidelines for evaporation modeling by other diffuse-interface models. Our work shows that deviations from the classical D^2 -Law are considerable for single droplet evaporation in finite-size systems ($L/D_0 < 5$). Such a criterion would also be informative for experimental work considering whether the setup is actually under conditions closer to an infinite or finite-size system. Further work will be focused on theoretical analysis for thermal multi-component droplet evaporation in finite-size systems and its modeling by appropriately extending the present numerical method.

ACKNOWLEDGMENTS

This work was supported by the Swiss National Science Foundation (Project No. 175793) and the Swiss National Super Computing Center (Projects No. s1081 and No. go09). L. Fei would like to thank Professor D. Sun at Southeast University for his helpful discussion on the shrinkage effect. K.H.L. would like to acknowledge support from the UK Engineering and Physical Sciences Research Council (EPSRC) under the project ‘‘UK Consortium on Mesoscale Engineering Sciences (UKCOMES)’’ (Grants No. EP/R029598/1 and No. EP/T015233/1).

APPENDIX A: 2D SINGLE-COMPONENT DROPLET EVAPORATION

With assumptions (i) and (ii) in Sec. II, the governing equation of the heat transport in cylindrical coordinates can be simplified as

$$\rho c_p v_r \frac{\partial T}{\partial r} = \frac{1}{r} \frac{\partial}{\partial r} \left(r \lambda \frac{\partial T}{\partial r} \right), \quad r \geq r_s, \quad (\text{A1})$$

where v_r is the velocity component in the radial direction. According to assumptions (iii) and (iv), the energy balance at the droplet surface is

$$\lambda \left. \frac{\partial T}{\partial r} \right|_{r=r_s} = \rho_s v_{r,s} h_{fg}. \quad (\text{A2})$$

Similarly, using the continuity equation ($r \rho v_r = r_s \rho_s v_{r,s}$) and Eq. (A2), by integrating Eq. (A1) from r_s to r , we can obtain

$$r_s \rho_s v_{r,s} [c_p (T - T_s) + h_{fg}] = r \lambda \frac{\partial T}{\partial r}. \quad (\text{A3})$$

By separating the variables and integrating Eq. (A3) from the droplet surface to the boundary, we obtained

$$r_s \rho_s v_{r,s} c_p \ln \left(\frac{r_2}{r_s} \right) = \lambda \ln(1 + B), \quad (\text{A4})$$

with $B = c_p (T_2 - T_s) / h_{fg}$. Substituting the continuity condition within the droplet ($\rho_s v_{r,s} = -\rho_l \partial r_s / \partial t$) and separating the variables, Eq. (A4) could be rewritten as

$$d \left[\frac{r_s^2}{2} \ln \left(\frac{r_2}{r_s} \right) + \frac{r_s^2}{4} \right] = -\frac{\lambda}{\rho_l c_p} \ln(1 + B) dt. \quad (\text{A5})$$

Integrating the above equation, the time evolution of D is described as

$$[\ln(L/D) + 1/2] D^2 = [\ln(L/D_0) + 1/2] D_0^2 - Kt, \quad (\text{A6})$$

where $K = \lambda / (\rho_l c_p) \ln(1 + B)$.

The temperature field could also be solved at a given time ($D = 2r_s$ is fixed), by defining the index $\xi_{2D} = \ln(1 + B) / \ln(L/D)$ and substituting it into Eq. (A3), which gives

$$\xi_{2D} \frac{1}{r} dr = \frac{dT}{(T - T_s + h_{fg}/c_p)}. \quad (\text{A7})$$

Integrating Eq. (A7) and after some standard derivations, we could finally obtain

$$T = \frac{h_{fg}}{c_p} \left[\left(\frac{r}{r_s} \right)^{\xi_{2D}} - 1 \right] + T_s, \quad r \geq r_s. \quad (\text{A8})$$

TABLE II. An example (based on Case 10) of the unit conversion.

Variables	L_m	T_m	K	t_m	Δx	ΔT	Δt
Lattice units	70	0.0143	0.0125	3.92×10^5	1	1.43×10^{-3}	1
Physical units	10^{-3} m	647 K	1.702×10^{-7} m ² /s	5.8 s	1.43×10^{-5} m	64.7 K	1.48×10^{-5} s

APPENDIX B: TWO-COMPONENT ISOTHERMAL EVAPORATION

For two-component isothermal evaporation [sketched in Fig. 1(b)], the theoretical solution could be derived based on similar assumptions: (i) the evaporation process is quasi-steady, (ii) ρD is constant, and (iii) the gas component β is insoluble in the droplet. The governing equation of component transport in spherical coordinates (3D) can be simplified as

$$\rho v_r \frac{\partial Y}{\partial r} = \frac{1}{r^2} \frac{\partial}{\partial r} \left(r^2 \rho D \frac{\partial Y}{\partial r} \right), \quad r \geq r_s, \quad (\text{B1})$$

where Y is the mass concentration for the droplet component, i.e., $Y = \rho_\alpha / \rho$, and $\rho = \rho_\alpha + \rho_\beta$ is the density of the mixture. According to Fick's law, the concentration balance at the droplet surface can be described as follows:

$$\rho D \frac{\partial Y}{\partial r} \Big|_{r=r_s} = -(1 - Y_s) \rho_{\alpha,s} v_{r,s}. \quad (\text{B2})$$

Using the continuity equation ($r^2 \rho v_r = r_s^2 \rho_{\alpha,s} v_{r,s}$) and Eq. (B2), by integrating Eq. (B1) from r_s to r , we can obtain

$$r_s^2 \rho_{\alpha,s} v_{r,s} (Y - 1) = r^2 \rho D \frac{\partial Y}{\partial r}. \quad (\text{B3})$$

By separating the variables and integrating Eq. (B2) from the droplet surface to the boundary, it is obtained as

$$r_s^2 \rho_{\alpha,s} v_{r,s} \left(\frac{1}{r_s} - \frac{1}{r} \right) = \rho D \ln(1 + B) \quad (\text{B4})$$

with $B = (Y_s - Y_2)/(1 - Y_s)$. According to assumption (iii), substituting the continuity condition within the droplet ($\rho_{\alpha,s} v_{r,s} = -\rho_l \partial r_s / \partial t$) and separating the variables, Eq. (B4) could be rewritten as

$$d \left[r_s^2 \left(\frac{1}{2} - \frac{r_s}{3r_2} \right) \right] = -\frac{\rho D}{\rho_l} \ln(1 + B) dt. \quad (\text{B5})$$

Integrating the above equation, the time evolution of D is obtained:

$$\left(1 - \frac{2D}{3L} \right) D^2 = \left(1 - \frac{2D_0}{3L} \right) D_0^2 - Kt, \quad (\text{B6})$$

where $K = (8\rho D / \rho_l) \ln(1 + B)$. It is seen from Eq. (B6) that for finite system sizes, the decrease of D^2 with t does not follow classical D^2 Law for two-component isothermal droplet evaporation expressed in Eq. (2).

The concentration field could also be solved at a given time ($D = 2r_s$ is known), by defining the index $\xi_{3D} =$

$\ln(1 + B)/(1 - D/L)$ and substituting it into Eq. (B3), we have

$$\xi_{3D} \frac{r_s}{r^2} dr = \frac{dY}{(Y - 1)}. \quad (\text{B7})$$

Integrating Eq. (B7) and after some standard derivations, we could finally get

$$Y = Y_{A,s} - \frac{\Delta Y}{B} \left\{ \exp \left[\xi_{3D} \left(1 - \frac{r_s}{r} \right) \right] - 1 \right\}, \quad r \geq r_s \quad (\text{B8})$$

with $\Delta Y = Y_s - Y_2$, which shows an exponential concentration profile outside the droplet.

Analogously, the time evolution of D for 2D two-component isothermal evaporation can be obtained:

$$[\ln(L/D) + 1/2]D^2 = [\ln(L/D_0) + 1/2]D_0^2 - Kt. \quad (\text{B9})$$

Correspondingly, the concentration profile at a given time ($D = 2r_s$ is known) is

$$Y = Y_{A,s} - \frac{\Delta Y}{B} \left[\left(\frac{r_s}{r} \right)^{\xi_{2D}} - 1 \right], \quad r \geq r_s, \quad (\text{B10})$$

where the index is defined as $\xi_{2D} = \ln(1 + B)/\ln(L/D)$.

APPENDIX C: CONVERSION FROM LATTICE TO PHYSICAL UNITS

A variable χ in lattice units (with subscript l) can be converted to the physical units (with subscript p) based on the correspondingly characteristic variable χ_m , i.e., $\chi_p = (\chi_{m,p} / \chi_{m,l}) \chi_l$. For the present study, we consider three primary characteristic variables, i.e., characteristic length (L_m), characteristic time (t_m), and characteristic temperature (T_m). Other characteristic variables can be defined accordingly, e.g., the characteristic velocity $u_m = L_m / t_m$. The characteristic length and temperature are chosen as the droplet initial diameter ($L_m = D_0$) and the critical temperature ($T_m = T_c$), respectively. The evaporation is driven by the temperature gradient (thermal diffusion), thus the characteristic time is defined as the diffusion time scale (droplet lifetime), $t_m = D_0^2 / K$. Taking the evaporation of a 1-mm water droplet as an example, the conversion from lattice to physical units for the first 3D case (Case 10 in Table I) is given in Table II. The evaporation constant K in the physical units is calculated based on thermophysical properties at 421 K: $\lambda = 0.6824$ W/(mK), $c_p = 4.304$ kJ/(kg K), $\rho_l = 919.2$ kg/m³, and $h_{fg} = 2121.1$ kJ/kg.

[1] C. K. Law, *Combustion Physics* (Cambridge University Press, Cambridge, 2010).

[2] B. Blocken and J. Carmeliet, Impact, runoff and drying of wind-driven rain on a window glass surface: numerical mod-

elling based on experimental validation, *Build. Environ.* **84**, 170 (2015).

[3] K. L. Chong, C. S. Ng, N. Hori, R. Yang, R. Verzicco, and D. Lohse, Extended Lifetime of Respiratory Droplets in a

- Turbulent Vapor Puff and Its Implications on Airborne Disease Transmission, *Phys. Rev. Lett.* **126**, 034502 (2021).
- [4] C. K. Law and H. K. Law, A D2-law for multicomponent droplet vaporization and combustion, *AIAA J.* **20**, 522 (1982).
- [5] C. K. Law and F. A. Williams, Kinetics and convection in the combustion of alkane droplets, *Combust. Flame* **19**, 393 (1972).
- [6] F. Qin, M. Su, J. Zhao, A. Mazloomi Moqaddam, L. Del Carro, T. Brunschwiler, Q. Kang, Y. Song, D. Derome, and J. Carmeliet, Controlled 3D nanoparticle deposition by drying of colloidal suspension in designed thin microporous architectures, *Int. J. Heat Mass Transf.* **158**, 120000 (2020).
- [7] F. Qin, A. Mazloomi Moqaddam, L. Del Carro, Q. Kang, T. Brunschwiler, D. Derome, and J. Carmeliet, Tricoupled hybrid lattice Boltzmann model for nonisothermal drying of colloidal suspensions in micropore structures, *Phys. Rev. E* **99**, 053306 (2019).
- [8] Q. Li, P. Zhou, and H. J. Yan, Pinning-depinning mechanism of the contact line during evaporation on chemically patterned surfaces: A lattice Boltzmann study, *Langmuir* **32**, 9389 (2016).
- [9] A. Mazloomi Moqaddam, D. Derome, and J. Carmeliet, Dynamics of contact line pinning and depinning of droplets evaporating on microribs, *Langmuir* **34**, 5635 (2018).
- [10] S. R. Turns *et al.*, *Introduction to Combustion*, Vol. 287 (McGraw-Hill, New York, NY, 1996).
- [11] N. Nishiwaki, Kinetics of liquid combustion processes: Evaporation and ignition lag of fuel droplets, *Symp. (Int.) Combust.* **5**, 148 (1955).
- [12] D. L. Dietrich, J. B. Haggard Jr, F. L. Dryer, V. Nayagam, B. D. Shaw, and F. A. Williams, Droplet combustion experiments in spacelab, *Symp. (Int.) Combust.* **26**, 1201 (1996).
- [13] C. L. A. Berli and M. G. Bellino, Extending lifetime of water droplets using mirror-nanoporous surfaces, *Adv. Mater. Interfaces* **8**, 1 (2021).
- [14] A. S. Rana, D. A. Lockerby, and J. E. Sprittles, Lifetime of a Nanodroplet: Kinetic Effects and Regime Transitions, *Phys. Rev. Lett.* **123**, 154501 (2019).
- [15] Y. Gong, G. Xiao, X. Ma, K. H. Luo, S. Shuai, and H. Xu, Phase transitions of multicomponent fuel droplets under sub- and supercritical conditions, *Fuel* **287**, 119516 (2021).
- [16] R. Ledesma-Aguilar, D. Vella, and J. M. Yeomans, Lattice-Boltzmann simulations of droplet evaporation, *Soft Matter* **10**, 8267 (2014).
- [17] H. Safari, M. H. Rahimian, and M. Krafczyk, Extended lattice Boltzmann method for numerical simulation of thermal phase change in two-phase fluid flow, *Phys. Rev. E* **88**, 013304 (2013).
- [18] H. Safari, M. H. Rahimian, and M. Krafczyk, Consistent simulation of droplet evaporation based on the phase-field multiphase lattice Boltzmann method, *Phys. Rev. E* **90**, 033305 (2014).
- [19] H. Yazdi, M. H. Rahimiani, and H. Safari, Numerical simulation of pressure-driven phase-change in two-phase fluid flows using the lattice Boltzmann method, *Comput. Fluids* **172**, 8 (2018).
- [20] Q. Li, K. H. Luo, Q. Kang, Y. L. He, Q. Chen, and Q. Liu, Lattice Boltzmann methods for multiphase flow and phase-change heat transfer, *Prog. Energy Combust. Sci.* **52**, 62 (2016).
- [21] K. H. Luo, L. Fei, and G. Wang, A unified lattice Boltzmann model and application to multiphase flows, *Philos. Trans. R. Soc. A* **379**, 20200397 (2021).
- [22] L. Chen, A. He, J. Zhao, Q. Kang, Z.-Y. Li, J. Carmeliet, N. Shikazono, and W.-Q. Tao, Pore-scale modeling of complex transport phenomena in porous media, *Prog. Energy Combust. Sci.* **88**, 100968 (2022).
- [23] H. Liu, Q. Kang, C. R. Leonardi, S. Schmieschek, A. Narváez, B. D. Jones, J. R. Williams, A. J. Valocchi, and J. Harting, Multiphase lattice Boltzmann simulations for porous media applications: A review, *Comput. Geosci.* **20**, 777 (2016).
- [24] Q. Li, Q. J. Kang, M. M. Francois, and A. J. Hu, Lattice Boltzmann modeling of self-propelled leidenfrost droplets on ratchet surfaces, *Soft Matter* **12**, 302 (2016).
- [25] F. Qin, L. Del Carro, A. Mazloomi Moqaddam, Q. Kang, T. Brunschwiler, D. Derome, and J. Carmeliet, Study of non-isothermal liquid evaporation in synthetic micro-pore structures with hybrid lattice Boltzmann model, *J. Fluid Mech.* **866**, 33 (2019).
- [26] W. Yuan and L. Zhang, Pinning-depinning mechanisms of the contact line during evaporation of micro-droplets on rough surfaces: A lattice Boltzmann simulation, *Langmuir* **34**, 8b00857 (2018).
- [27] L. Y. Shen, G. H. Tang, Q. Li, and Y. Shi, Hybrid wettability-induced heat transfer enhancement for condensation with noncondensable gas, *Langmuir* **35**, 9430 (2019).
- [28] S. Zheng, F. Eimann, C. Philipp, T. Fieback, and U. Gross, Single droplet condensation in presence of noncondensable gas by a multi-component multi-phase thermal lattice Boltzmann model, *Int. J. Heat Mass Transf.* **139**, 254 (2019).
- [29] R. Huang, H. Wu, and N. A. Adams, Mesoscopic Lattice Boltzmann Modeling of the Liquid-Vapor Phase Transition, *Phys. Rev. Lett.* **126**, 244501 (2021).
- [30] D. Albernaz, M. Do-Quang, and G. Amberg, Multirelaxation-time lattice Boltzmann model for droplet heating and evaporation under forced convection, *Phys. Rev. E* **91**, 043012 (2015).
- [31] S. T. Chang and O. D. Velev, Evaporation-induced particle microseparations inside droplets floating on a chip, *Langmuir* **22**, 1459 (2006).
- [32] C. Verwey and M. Birouk, Experimental investigation of the evaporation of suspended mono-sized heptane droplets in turbulence intensities approaching unity, *Combust. Flame* **219**, 425 (2020).
- [33] Y.-H. Qian, D. d'Humières, and P. Lallemand, Lattice BGK Models for Navier-Stokes Equation, *EPL (Europhysics Lett.)* **17**, 479 (1992).
- [34] S. Chen and G. D. Doolen, Lattice Boltzmann method for fluid flows, *Annu. Rev. Fluid Mech.* **30**, 329 (1998).
- [35] S. Succi, *The Lattice Boltzmann Equation: For Complex States of Flowing Matter* (Oxford University Press, Oxford, 2018).
- [36] Y. Gan, A. Xu, G. Zhang, and S. Succi, Discrete Boltzmann modeling of multiphase flows: hydrodynamic and thermodynamic nonequilibrium effects, *Soft Matter* **11**, 5336 (2015).
- [37] C. Lin, K. H. Luo, A. Xu, Y. Gan, and H. Lai, Multiple-relaxation-time discrete Boltzmann modeling of multicomponent mixture with nonequilibrium effects, *Phys. Rev. E* **103**, 013305 (2021).
- [38] H. Liu, Y. Lu, S. Li, Y. Yu, and K. C. Sahu, Deformation and breakup of a compound droplet in three-dimensional oscillatory shear flow, *Int. J. Multiph. Flow* **134**, 103472 (2021).
- [39] N. Wang, C. Semperebon, H. Liu, C. Zhang, and H. Kusumaatmaja, Modelling double emulsion formation in planar flow-focusing microchannels, *J. Fluid Mech.* **895**, A22 (2020).

- [40] H. Liu, Y. Ba, L. Wu, Z. Li, G. Xi, and Y. Zhang, A hybrid lattice Boltzmann and finite difference method for droplet dynamics with insoluble surfactants, *J. Fluid Mech.* **837**, 381 (2018).
- [41] M. Geier, A. Greiner, and J. G. Korvink, Cascaded digital lattice Boltzmann automata for high reynolds number flow, *Phys. Rev. E* **73**, 066705 (2006).
- [42] L. Fei and K. H. Luo, Consistent forcing scheme in the cascaded lattice Boltzmann method, *Phys. Rev. E* **96**, 053307 (2017).
- [43] L. Fei, K. H. Luo, and Q. Li, Three-dimensional cascaded lattice Boltzmann method: Improved implementation and consistent forcing scheme, *Phys. Rev. E* **97** 053309, (2018).
- [44] L. Fei, J. Du, K. H. Luo, S. Succi, M. Lauricella, A. Montessori, and Q. Wang, Modeling realistic multiphase flows using a nonorthogonal multiple-relaxation-time lattice Boltzmann method, *Phys. Fluids* **31**, 042105 (2019).
- [45] A. K. Gunstensen, D. H. Rothman, S. Zaleski, and G. Zanetti, Lattice Boltzmann model of immiscible fluids, *Phys. Rev. A* **43**, 4320 (1991).
- [46] D. Grunau, S. Chen, and K. Eggert, A lattice Boltzmann model for multiphase fluid flows, *Phys. Fluids A* **5**, 2557 (1993).
- [47] X. Shan and H. Chen, Lattice Boltzmann model for simulating flows with multi phases and components, *Phys. Rev. E* **47**, 1815 (1993).
- [48] X. W. Shan and H. D. Chen, Simulation of nonideal gases and liquid-gas phase-transitions by the lattice Boltzmann equation, *Phys. Rev. E* **49**, 2941 (1994).
- [49] M. R. Swift, W. R. Osborn, and J. M. Yeomans, Lattice Boltzmann Simulation of Nonideal Fluids, *Phys. Rev. Lett.* **75**, 830 (1995).
- [50] M. R. Swift, E. Orlandini, W. R. Osborn, and J. M. Yeomans, Lattice Boltzmann simulations of liquid-gas and binary fluid systems, *Phys. Rev. E* **54**, 5041 (1996).
- [51] X. He, S. Chen, and R. Zhang, A lattice Boltzmann scheme for incompressible multiphase flow and its application in simulation of rayleigh-taylor instability, *J. Comput. Phys.* **152**, 642 (1999).
- [52] M. Sugimoto, Y. Sawada, M. Kaneda, and K. Suga, Consistent evaporation formulation for the phase-field lattice Boltzmann method, *Phys. Rev. E* **103**, 053307 (2021).
- [53] L. Fei, J. Yang, Y. Chen, H. Mo, and K. H. Luo, Mesoscopic simulation of three-dimensional pool boiling based on a phase-change cascaded lattice Boltzmann method, *Phys. Fluids* **32**, 103312 (2020).
- [54] P. Yuan and L. Schaefer, Equations of state in a lattice Boltzmann model, *Phys. Fluids* **18**, 042101 (2006).
- [55] Q. Li, Q. J. Kang, M. M. Francois, Y. L. He, and K. H. Luo, Lattice Boltzmann modeling of boiling heat transfer: the boiling curve and the effects of wettability, *Int. J. Heat Mass Transf.* **85**, 787 (2015).
- [56] Q. Li, K. H. Luo, and X. J. Li, Lattice Boltzmann modeling of multiphase flows at large density ratio with an improved pseudopotential model, *Phys. Rev. E* **87**, 053301 (2013).
- [57] Q. Li, K. H. Luo, and X. J. Li, Forcing scheme in pseudopotential lattice Boltzmann model for multiphase flows, *Phys. Rev. E* **86**, 016709 (2012).
- [58] S. Saito, A. de Rosis, L. Fei, K. H. Luo, K. I. Ebihara, A. Kaneko, Y. Abe, and K. Koyama, Lattice Boltzmann modeling and simulation of forced-convection boiling on a cylinder, *Phys. Fluids* **33**, 023307 (2021).
- [59] P. Yue, C. Zhou, and J. J. Feng, Spontaneous shrinkage of drops and mass conservation in phase-field simulations, *J. Comput. Phys.* **223**, 1 (2007).
- [60] L. Zheng, T. Lee, Z. Guo, and D. Rumschitzki, Shrinkage of bubbles and drops in the lattice Boltzmann equation method for nonideal gases, *Phys. Rev. E* **89**, 033302 (2014).
- [61] C. Zhang and Z. Guo, Spontaneous shrinkage of droplet on a wetting surface in the phase-field model, *Phys. Rev. E* **100**, 061302 (2019).
- [62] Q. Zou and X. He, On pressure and velocity flow boundary conditions and bounceback for the lattice Boltzmann BGK model, *Phys. Fluids* **9**, 1591 (1997).
- [63] Z. Guo, C. Zheng, and B. Shi, Nonequilibrium extrapolation method for velocity and pressure boundary conditions in the lattice Boltzmann method, *Chinese Phys.* **11**, 366 (2002).
- [64] T. Lee and P. F. Fischer, Eliminating parasitic currents in the lattice Boltzmann equation method for nonideal gases, *Phys. Rev. E* **74**, 046709 (2006).